Melt pond fraction and spectral sea ice albedo retrieval from MERIS data I: validation against in situ, aerial, and ship cruise data

L. Istomina[1], G. Heygster[1], M. Huntemann[1], P. Schwarz[2], G. Birnbaum[3], R. Scharien[4], C. Polashenski[5], D. Perovich[5], E. Zege[6], A. Malinka[6], A. Prikhach[6] and I. Katsev[6]

[1]{Institute of Environmental Physics, University of Bremen, Bremen, Germany}

[2]{Department of Environmental Meteorology, University of Trier, Trier, Germany}

[3]{Alfred Wegener Institute, Helmholtz Centre for Polar and Marine Research, Bremerhaven, Germany}

[4]{Department of Geography, University of Victoria, Victoria, Canada}

[5]{Cold Regions Research and Engineering Laboratory, Engineer Research and Development Center, Hanover, New Hampshire, USA}

[6]{B.I. Stepanov Institute of Physics, National Academy of Sciences of Belarus, Minsk, Belarus}

Correspondence to: L. Istomina (lora@iup.physik.uni-bremen.de)

Abstract

The presence of melt ponds on the Arctic sea ice strongly affects the energy balance of the Arctic Ocean in summer. It affects albedo as well as transmittance through the sea ice, which has consequences for the heat balance and mass balance of sea ice. An algorithm to retrieve melt pond fraction and sea ice albedo from MEdium Resolution Imaging Spectrometer (MERIS) data is validated against aerial, ship borne and in situ campaign data. The results show the best correlation for landfast and multiyear ice of high ice concentrations. For broadband albedo R^2 is equal to 0.85, with the RMS being equal to 0.068, for the melt pond

fraction: R^2 is equal to 0.36 with the RMS being equal to 0.065. The correlation for lower ice concentrations, subpixel ice floes, blue ice and wet ice is lower due to ice drift and challenging for the retrieval surface conditions. Combining all aerial observations gives a mean albedo RMS of 0.089 and a mean melt pond fraction RMS of 0.22. The in situ melt pond fraction correlation is R^2=0.52 with an RMS=0.14. Ship cruise data might be affected by documentation of varying accuracy within the Antarctic Sea Ice Processes and Climate (ASPeCt) protocol, which may contribute to the discrepancy between the satellite value and the observed value: mean R^2=0.044, mean RMS=0.16. An additional dynamic spatial cloud filter for MERIS over snow and ice has been developed to assist with the validation on swath data.

1 Introduction

Melt ponds on the Arctic sea ice affect the albedo, mass balance and heat balance of the ice (e.g. Perovich et al., 2009) by translating the increase of air temperature into drastic and rapid surface type changes. They introduce a positive feedback within the sea ice albedo feedback loop (Curry et al., 1995) thus facilitating further ice melt. In the context of changing Arctic climate (Shindell and Faluvegi, 2009), knowledge of melt pond fraction (MPF), its spatial distribution and the length of the melt season is required to reflect and predict the role of the sea ice cover in the radiative balance of the region. Schröder et al. (2014) show the potential of predicting the minimum sea ice extent in autumn by the spring MPF. In addition to applications in climate studies, e.g. global circulation modeling, knowledge of the MPF can be helpful for navigation purposes. Findings from numerous in situ campaigns (Barber and Yackel, 1999; Hanesiak et al., 2001; Yackel et al., 2000) provide data of excellent quality and detail, but unfortunately lack in coverage. To fill in this gap, a remote sensing approach needs to be employed.

The present work is dedicated to validation of a MPF and sea ice albedo retrieval algorithm, the Melt Pond Detector (MPD), described by Zege et al. (2015). The algorithm differs from existing satellite remote sensing algorithms, e.g. Rösel et al. (2012) or Tschudi et al. (2008), by 1) utilizing a physical model of sea ice and melt ponds with no a priori surface spectral relectances, and 2) providing daily averaged MPF instead of weekly averaged MPF, which is beneficial in case of rapid melt evolution. Field observations (Figure 1) show faster melt

evolution on first year ice (FYI) as compared to multiyear ice (MYI). Due to the fact that MPF depends not only on air temperature and available melt water volume but also on the ice topography (Eicken et al., 2004; Polashenski et al., 2012), the melt evolution is different for FYI and MYI. Melt onset proceeds rapidly to the MPF maximum on FYI with rapid pond drainage and moderate MPFs afterwards. On multiyear ice, the evolution of melt up to the melt maximum takes longer. The peak MPF value is lower and the MPF decrease is slower than that on FYI (Figure 1). A detailed description of melt stages and melt water distribution mechanisms can be found in Polashenski et al. (2012). These details of melt evolution are responsible for the spatial variability of MPF and sea ice albedo. The temporal variability of MPF is driven by air mass transport and changing air temperature. This introduces complications in the MPF modeling and creates the need for an MPF and sea ice albedo dataset of possibly high temporal and spatial resolution, which can be retrieved from satellite data.

The manuscript is structured as follows: in Section 2 the MPD algorithm, its input and output data are described. Section 3 is dedicated to validation of the cloud screening (Sect. 3.1), albedo (Sect. 3.2) and MPF (Sect. 3.3) products. The additional cloud screening developed for the purpose of quality validation is presented in Section 3.3.2. The conclusions are given in Section 4.

2 Data used

The data used for the present study are the pond fraction and broadband sea ice albedo swath data products retrieved from MERIS swath Level 1b data over the ice covered Arctic Ocean using the MPD retrieval. The present chapter presents a short summary of the MPD retrieval. The full description of the algorithm can be found in Zege et al. (2015).

The MPD is an algorithm for retrieving characteristics (albedo and melt ponds fraction) of summer melting ice in the Arctic from data of satellite spectral instruments. In contrast to previously developed algorithms (Rösel et. al, 2012; Tschudi et al., 2008) MPD does not use a priori values of the spectral albedo of constituents of the melting ice (melt ponds, drained surface, etc.).

The retrieval algorithm is based on the observations of optical properties of constituents of sea-ice (Perovich, 1996). A sea ice pixel is considered as consisting of two components: white

ice and melt ponds. The reflection properties of surface are described by the spectral bi-directional reflectance distribution function (BRDF) $R(\theta, \theta_0, \varphi, \lambda)$, where θ and θ_0 are the zenith angles of the observation and illumination directions, respectively, and φ is the azimuth angle between them, λ is the wavelength.

The white ice is considered as an optically thick weakly absorbing layer. The BRDF of this sub-pixel $R_{ice}(\theta, \theta_0, \varphi, \lambda)$ is determined by its optical depth τ_{wi}, the mean effective grain size a_{eff}, and the absorption coefficient α_{yp} of yellow pigments, which could arise due to sediments suspended in the seawater. The spectral dependencies of optical characteristics of a layer are determined by the spectrum of the complex refractive index of ice by (Warren and Brandt, 2008) and spectral absorption of yellow pigments by (Bricaud et al., 1981). The used analytical approximation for $R_{ice}(\theta, \theta_0, \varphi, \lambda)$ has been developed on the base of the asymptotic solution of the radiative transfer theory (Zege et al., 1991).

The BRDF of a melt pond $R_{pond}(\theta, \theta_0, \varphi, \lambda)$ is determined by the melt water optical depth τ_p and by the spectral albedo of its bottom. The pond bottom is an ice layer, which in turn is characterized by the transport scattering coefficient σ_{ice} and the optical depth τ_{ice}. Thus, the BRDF of the melt pond is calculated as reflection of the water layer with a semi-translucent bottom.

It is supposed that the pixel surface consists of white ice (highly reflective) and melt ponds with area fraction *S*. The BRDF of the whole pixel is a linear combination:

$$R(\theta, \theta_0, \varphi, \lambda) = (1 - S)R_{ice}(\theta, \theta_0, \varphi, \lambda) + SR_{pond}(\theta, \theta_0, \varphi, \lambda) \quad (1)$$

The body of the retrieval algorithm comprises of the following steps.

1. The input to the algorithm is the MERIS level 1B data, including the radiance coefficients R_i at channels *i*=1, 2, 3, 4, 8, 10, 12, 13, 14 (correspond to the central wavelengths of 412.5, 442.5, 490, 510, 681.25, 753.75, 778.75, 865 and 885nm), and the solar and observation angles (zenith and azimuth). Also the relevant information on atmosphere and surface state can be entered from an input file.

2. The data is sent to the three independent blocks:

a. The atmospheric correction preprocessing block. The atmosphere reflectance r_i and transmittance t_i are calculated for the used set of wavelengths (i is the channel number). Atmospheric correction is performed with regard to the surface BRDF.

b. Separation of the sea-ice pixels. In this procedure the ice pixels are separated from the cloud, land and open water pixels, using a brightness criterion on the channels R_2, R_3, and R_4, spectral neutrality criterion on the ratio of the channels R_1 and R_2, MERIS differential snow index (Schlundt et al., 2011) and the threshold on the ratio of the MERIS oxygen-A band (R_{11} and R_{10}). The first two criteria separate white surfaces, which can be snow, ice, or cloud. The MERIS differential snow index and oxygen-A band threshold discard cloudy pixels over snow.

c. Setting the bounds for ice and pond parameters. These border values serve to stabilize the algorithm and are set to correspond to values observed in nature (obtained by analyzing the field data from the Polarstern cruise (Istomina et al., 2013) and from the CRREL field observations (Polashenski et al., 2012)).

3. The main part of the algorithm is an iterative procedure to retrieve ice and pond parameters and the pond fraction *S*. The procedure is based on the Newton-Raphson method (Press et al., 1987) that provides the search of the minimum of the functional $\sum_i (R_i^{meas} - R_i^{calc})^2$ in the space of ice and ponds characteristics and fraction *S*.

4. The resulting characteristics and the value of *S* are used to calculate the spectral albedo of the pixel.

5. Output is the melt pond area fraction, the spectral albedo, and the estimation of the retrieval error in the pixel. The spectral albedo is retrieved at six wavelengths specified by the user. For the validation studies presented in this paper, the broadband sea ice albedo has been calculated as an average of the six spectral albedo values at 400-900nm in steps of 100nm.

A satellite scene is processed pixel by pixel, producing an hdf5-formatted map of output values.

The MPD algorithm has been preliminarily verified numerically, using a synthetic dataset of top of atmosphere radiances from melting Arctic ice as the input of a satellite spectral instrument. This dataset was computed with software developed based on the radiative transfer code RAY (Tynes et al., 2001; Kokhanovsky et al., 2010) for calculating signals reflected by the melting sea ice-atmosphere system. Thus the radiances in the MERIS spectral channels were simulated for a set of ice pixels for a few typical situations, including 'standard' white ice, bright ice (snow covered), dark and light blue melt ponds. The numerical experiment showed that the melt pond fraction can be retrieved with high accuracy (error less than 1%) for the most common case of 'standard' white ice and light blue (young) melt pond. The retrieval error increases with deviation from the 'standard' case, e.g. the retrieved pond fraction can be underestimated more than twice for the case of bright (snow covered) ice and dark (mature) melt pond. However, this situation is rare, because in the case of an open (exposed) mature pond snowfall only affects the surrounding ice surface for a short time due to melt temperature. The case of lid covered melt pond is a separate topic, which is discussed in detail in Sect. 3.3.3. Submerged sea ice or water saturated ice surface are optically identical to melt ponds and are retrieved as such. At the same time the MPD algorithm provides accurate retrievals of the spectral albedo in all considered cases, even in the situations when the error of the pond fraction retrieval is high. The spectral albedo is retrieved much better with the MPD algorithm than with the conventional algorithms using the Lambert approximation for surface reflection, which underestimates the albedo at about 0.05 all over the spectral range, whereas the error of the MPD retrieval in the worst case ('bright ice – dark pond') is 0.01 and lower in all other considered cases.

3 Validation

The datasets used for the validation of the MPD algorithm are shown in Table 1.

These validation datasets contain a wide range of pond fractions and were obtained over landfast ice, FYI and MYI of various ice concentrations. Therefore the performance of the satellite retrieval can be thoroughly tested for a variety of conditions and conclusions on the more or less suitable conditions for the application of the MPD retrieval can be drawn. Such conclusions are especially important as the MPD retrieval was initially designed for a limited set of ice and pond parameters, namely for the conditions of the melt evolution with open

melt ponds surrounded by dry white ice within the pack ice. A sensitivity study based on modeled input data shows the algorithm's better performance for bright melt ponds as opposed to dark melt ponds (Zege et al., 2015). Therefore, it is expected that the MPD algorithm shows the best performance over MYI of high ice concentrations. The performance over lower ice concentrations, in case of subpixel ice floes, saturated wet dark ice or thin ponded ice is compromised due to the limitations of the retrieval (Zege et al., 2015). We, however, perform the comparison to the in situ data for all available conditions anyway in order to evaluate the performance of the algorithm at the global scale.

Unfortunately, MERIS only features VIS and NIR channels, whereas for effective cloud screening over snow, IR and TIR channels would be more suitable. Therefore MERIS is not the best instrument for cloud screening over snow and ice, and there remains a risk of cloud contamination in the swath data and final gridded product. To avoid this, an additional cloud screening (Sect. 3.3.2) was implemented which proved to give a much better result on swath data. For the gridded product, a restriction on the amount of valid data pixels to form one grid cell was applied to screen out cloud edges. These issues will be addressed below.

The summary of dataset locations is shown in Figure 2. Among the above mentioned datasets, the airborne measurements and transect estimates are more accurate than visual estimations; in case of ship cruise bridge observations or visual estimations of melt ponds fraction in the field, the measurement accuracy is hard to evaluate.

3.1 Validation of the cloud screening

In order to test the performance of the cloud screening presented in Zege et al. (2015), we have employed data from the AATSR sensor aboard the same satellite platform. The advantage of this sensor is that it has suitable IR channels for cloud screening over snow and ready procedures to perform this task. For this study, a cloud screening method for AATSR developed by Istomina et al. (2010) is used. For that, the swath data of both MERIS and AATSR was collocated and cut down to only AATSR swath. Then, the two cloud masks (the reference mask by AATSR and test mask by MERIS) have been compared as follows: for each swath, an average pond fraction in cloud free areas as seen by AATSR (Figure 3, blue curve) and by MERIS (Figure 3, red curve) has been derived. This has been done for the

period from May 1, 2009 to September 30, 2009. The resulting Figure 3 shows the effect of clouds on the MERIS MPD swath data: before the melt season, clouds have lower albedo than the bright surface and may be seen as melt ponds by the MPD retrieval. In the case of developed melt, the situation is the opposite: the melting surface is darker than clouds, and unscreened clouds are taken as lower pond fraction by the retrieval. Overall, the unscreened clouds in the MPD product result in smoothing out of the pond fraction toward the mean value of about 0.15. However, the temporal dynamics is preserved even in swath data. Partly the problem of unscreened clouds can be solved at the stage of gridding swath data into daily or weekly averages, by constraining the amount of valid pixels that form a valid grid cell so that cloudy areas which are only partly unscreened in the swath data are still not included in the gridded data (see Sect. 2 in the companion paper Istomina et al., 2015). It is important to note the positive MPF bias even in the data cloud screened with the reference AATSR cloud mask (blue curve in Figure 3) both in May and in September 2009 where no melt ponds should be present. One of the reasons for the bias in September might be the specifics of the MPD retrieval which detects also frozen ponds as MPF (see Sect. 3.3.3 for details). Another reason might be the actual accuracy issues of the MPD retrieval for dark ponds (see Zege et al. (2015) for details). Given the geographical coverage of the study region (Arctic Ocean to the north of 65°N), the positive MPF bias in May can appear due to water saturated sea ice (after the onset of positive air temperature but before the actual widespread melt).

3.2 Validation of the albedo product

3.2.1 In situ validation

Validation of the sea ice albedo satellite retrieval is a non-trivial task due to high spatial variability. In summer this variability is even more pronounced as each given duration and intensity of melt or refreeze creates an optically unique surface type (various grain sizes of sea ice and snow, drained, forming, overfrozen melt ponds, deep or shallow ponds on MYI or FYI, intermediate slushy areas, etc). For a satellite pixel size of 1.2 km x 1.2 km the surface types and their fractions from field observations are in the best case only known for a 100-200 m long transect. In order to obtain the in situ sea ice albedo, a linear mix of all surface

fractions is constructed. The availability of such comprehensive field measurements is very limited, and for those available, the question of how representative the chosen transect is for the whole area is anyway present. In this study, we use a transect data taken in the Canadian Arctic in June and July 2006 as part of the joint Finnish Institute of Marine Research and University of Calgary Cryosphere Climate Research Group polar ice POL-ICE research project (Geldsetzer et al., 2006), where the uniform pond distribution was confirmed using helicopter images (not shown here).

During POL-ICE 2006 the spatio-temporal evolution of surface features and their spectral reflectance properties were monitored by collecting a series of transect measurements on landfast FYI (FI) also in the vicinity of Resolute Bay, Nunavut between June 26, 2006 and July 11, 2006. For each transect, a 200m transect line was established perpendicular to the predominant major-axis pond direction to maximize the frequency of changes between ponds and snow/bare ice patches. For the relatively uniformly distributed network of ponds and snow/bare ice patches characteristics of smooth FYI, this orientation yields a representative areal fraction of cover types (Grenfell and Perovich, 2004). A total of 12 transects were collected with surface cover types classified as: melt pond, snow/bare ice, or mixed at 0.5 m intervals. The mixed cover type was introduced to classify the slushy mixture of water saturated ice that could be neither classed as discrete pond or snow/bare ice. The data is shown in Table 2.

For 8 of POL-ICE 2006 transects when lighting conditions were suitable, cosine-corrected downwelling and upwelling radiance (0.35 m height) measurements were made at 2m intervals using a TriOS RAMSES spectrometer (320-950nm). Spectral data were processed using the calibration files and software bundled with the RAMSES spectrometer, with radiation measurements integrated across the bandwidth of the instrument to create integrated albedo measurements from each sample. Each albedo measurement was matched to a surface class, and average broadband albedo statistics by class and for each transect were derived. For these locations, the MPD retrieval has been performed and the broadband albedo average within 5km around the location has been produced. Satellite overflights closest in time to the field measurements were taken. The result is shown in Table 3, the comparison itself in the last column „Results“. The NaNs in the retrieved data are gaps due to cloud cover. Only four cases were cloud free. Overall, slight overestimation of the satellite albedo is visible. The

discrepancies between the field and satellite albedo can be explained by difference in the spatial resolution of the two datasets and varying melt pond distribution within the studied area.

3.2.2 Aerial validation

The validation has been performed for selected cloud free satellite swaths at the reduced resolution of the retrieval (MERIS data, reduced resolution, 1.2 km x 1.2 km).

The aircraft campaign MELTEX („Impact of melt ponds on energy and momentum fluxes between atmosphere and sea ice“) was conducted by the Alfred Wegener Institute for Polar and Marine Research (AWI) in May and June 2008 over the southern Beaufort Sea (Birnbaum et al., 2009).

The campaign aimed at improving the quantitative understanding of the impact of melt ponds on radiation, heat, and momentum fluxes over Arctic sea ice. For determining broadband surface albedo, the BASLER BT-67 type aircraft POLAR 5 was equipped with two Eppley pyranometers of type PSP measuring the broadband hemispheric down- and upwelling shortwave radiation. The radiation sensors were mounted on the aircraft in a fixed position. For clear-sky conditions, data of the upward facing pyranometer, which receives direct solar radiation, were corrected for the misalignment of the instrument (based on a method described by Bannehr & Schwiesow, (1993)) and the roll and pitch angles of the aircraft to derive downwelling hemispheric radiation flux densities for horizontal exposition of the sensor (see Lampert et al., 2012).

Weather conditions in May 2008 were characterized by warming events interrupted by cold-air advection from the inner parts of the Arctic towards the coast of the southern Beaufort Sea. A warming event on May 23 and May 24, 2008, caused the onset of melt pond formation on ice in a large band along the coast from the Amundsen Gulf to Alaska. On May 26, 2008, numerous melt ponds in a very early stage of development were overflown. However, from May 27 to June 1, 2008, a new period with prevailing cold-air flow caused a refreezing of most melt ponds, which were still very shallow at that time. During the last week of the measurements, a tongue of very warm air was shifted from Alaska to the Beaufort Sea. It

reached its largest extension over the ocean on June 4 and June 5, 2008, which again strongly forced the development of melt ponds.

The available validation data consist of 5 flight tracks for 5 days on May 26, and June 3, June 4, June 6 and June 7, 2008. Only the cloud free data is selected. The measurements were performed at different altitudes, as low as 50m and reaching 400m, with correspondingly different numbers of measurement points for each satellite pixel. The collocation of such an uneven dataset with the satellite data has been performed by calculating an orthodromic distance of every pixel within a satellite swath to a given aerial measurement point, and collecting those aerial points lying at the minimum distance to the centre of a given satellite pixel. This ensures that aerial measurements performed at any height are collocated to the corresponding satellite pixel correctly. The number of data points per flight is in the order of tens to hundreds of thousands with up to 500 points per satellite pixel.

The validation effort has been done on swath satellite data. The quality of retrieval conditions for the MPD algorithm differs for each overflight depending on weather conditions, ice concentration and ice type. In addition, time difference between the satellite overflight and aerial measurements affect the comparison (Table 4) due to ice drift.

An example of such different conditions is shown in Figure 4, where the flight tracks over FI and over separate ice floes are shown.

The time difference between the aerial measurement and satellite overflight varies for the presented cases, which adds to the validation data uncertainty for cases with lower ice concentrations due to drifting separate floes. Where possible in case of drift, the time difference was limited to 1.5 hours around the satellite overflight. Two exceptions with time difference 2^h-3^h are marked in Table 4. Figure 5 shows the altitude and the correlation of the measured and retrieved broadband albedo for the only flight over FI on June 06, 2008. The rest of the flights were flown over separate floes. As no screening of albedo data was possible, it was decided to limit the time difference to 1.5 hour around the satellite overflight for the asymmetrically distributed flights. Some points of low measured albedo but high retrieved albedo feature time difference up to 2h and are most probably connected to the drift of separate ice floes. These are flights on June 04, 2008, May 26, 2008, June 03, 2008 and June 07, 2008. They are shown in Figure 6, Figure 7 and Figure 8. Due to ice drift, the aerial

measurements are displaced relative to the satellite snapshot which causes different areas to be compared to each other. The resolution differences of the two sensors may increase this difference even more. Therefore, slight over or underestimation due to the ice concentration difference of aerial and satellite measurements is visible. As the numerical experiment shows that accuracy of the albedo retrieval in all cases is high (Zege et al., 2015), and the case of no drift shows high correlation of retrieved and measured albedo (fast ice (FI) case shown in Figure 5), we conclude that the discrepancy is due to the specifics of data used for validation and not a weak point of the MPD retrieval. To conclude, the best correlation for albedo retrieval is observed for the landfast ice, which are the conditions of the best algorithm performance with R^2=0.85, RMS=0.068. Due to the lack of field data the validation has not been performed over MYI, however, the MPD has been designed for MYI, namely sea ice of high concentration with light melt ponds. FI is a deviation from this case at least in the melt pond type, and potentially in the surface albedo, but as MPD performed well even in this case, we expect it‘s performance to be at least as good over MYI of high ice concentrations. Correlation for lower ice concentrations, subpixel ice floes, blue ice and wet ice is lower due to complicated surface conditions and ice drift. Combining all aerial observations gives a mean albedo RMS of 0.089.

3.3 Validation of the melt pond product

3.3.1 Aerial validation

For the validation of the melt pond product, the aerial photos from the same airborne campaign MELTEX 2008 have been used. Although the flight tracks are the same, the criteria for data selection are different for albedo and melt pond measurements. This is why the validation data for melt pond and albedo data not to overlap entirely for the same flight. The number of points per flight is in the order of hundreds with about 5 images per satellite pixel (example photograph is shown in Figure 9). Additionally, one more flight over MYI near the coast of North Greenland during the aerial campaign NOGRAM-2 2011 has been used.

For the evaluation of the aerial photographs a supervised classification method (maximum likelihood) was applied. For every pixel x, the probability *D* of belonging to every class c is calculated. The pixels get assigned to the class with the highest probability (Jensen, 2008). If

the training data is normally distributed, the maximum likelihood is expressed as follows (Gonzalez and Woods, 2002):

$$D = \ln(a_c) - [0.5 \ln(|Cov_c|)] - [0.5(X - M_c)^T (Cov_c^{-1})(X - M_c)]. \quad (2)$$

where D is the quantities weighted distance (likelihood), c is a particular class, X is the measurement vector of the candidate pixel, M_c is the mean vector of the sample of class c, a_c is the a priori probability of class c (set to equal values for all classes), Cov_c is the covariance matrix of the pixels in the sample of class c, T is the transposition function.

More than 10,000 aerial photographs were recorded during the MELTEX campaign during the different flight tracks. As the quality of the data was not uniform, only images which meet the following requirements were chosen: images taken during horizontal flight tracks (to minimize the geometric distortions) and clear sky flight tracks (to prevent a wrong classification because of fog, clouds and shadows of the clouds). The camera was operated with a non-constant exposure, so that the sea ice in images with a large fraction of open water was overexposed and useless for further evaluation. To simplify the automated classification, images of each day were separated into different flight tracks with similar exposure, ice conditions and same flight level. Nevertheless almost 3000 images were classified and evaluated for the MELTEX campaign. Two suitable flight tracks of the NOGRAM-2 campaign that contain about 1000 images were chosen to complement the quantification of the melt stages. Depending on the flight level, each image covered an area between 0.2 km^2 and 3 km^2.

Overall the validation data used features four types of sea ice: thin and thick FYI as well as FI for the MELTEX images, and MYI for NOGRAM-2. Most of the investigation area of the MELTEX campaign was covered by thin FYI or FI. Only on June 07, 2008, the most northerly part of the flight track contained a notable amount of thick FYI. This part showed a different behavior during the melting process and contained different surface classes than the thin FYI or FI.

Most flight tracks of the campaign were subdivided in several subflight tracks. For every subflight track a representative image was chosen, which contained all classes. In cases where there were no representative images with all classes for a given subflight track, two or more images were merged for the determination of the training data. The threshold for the

maximum likelihood method was set to 0.95. This means that the probability of belonging to a defined class must be 0.95 or higher. Otherwise the pixels were not classified. Within the presented study, the amount of unclassified pixels per image is uniformly about 1-2%.

The sea ice conditions varied greatly for each of the studied flights, with the cases ranging from land fast ice of 100% ice concentration, separate drifting ice floes to brash ice with subpixel ice floes (example in Figure 10). The cases with no separate ice floes and no ice drift are shown in Figure 11 (FI) and Figure 12 (left panel, MYI) with quite good correspondence of the retrieved and measured pond fractions. Right panel in Figure 12, on the other hand, shows higher retrieved MPF than measured from the aircraft. The reason for this discrepancy is twofold: relatively large time difference and the challenging surface conditions. The surface state at the time was as follows: the reported cold air intrusion in the area on June 01, 2008 prevented the forming melt ponds from evolving further (an overview on surface conditions in the area can be found in Scharien et al. (2012)), and the large floes were covered with frozen ponds at the beginning of their evolution. Frozen shallow ponds at the beginning of their evolution were classified as sea ice from the aerial images, but retrieved as melt ponds from the satellite. For the applications connected to the radiation budget studies (e.g., GCM), a generalization where darker types of sea ice and melt ponds are put into one class is appropriate due to similar radiative characteristics of the two.

Figure 13 shows the flight on June 07, 2008, which features larger ice floes than the flights shown in Figure 14. The MPF output of the MPD algorithm is not affected by the subpixel fraction of open water because the almost constant spectrum of open water only affects the amplitude and not the spectral shape of the mixture of surfaces (sea ice, ponds and open water) within the pixel; however, the spectral signature of melt ponds is harder to resolve in case of lower ice concentrations. Subpixel ice floes, brash ice, blue ice are not appropriate conditions for the MPD algorithm application, hence the overestimated pond fraction for both flights in Figure 14. Overall, the best correlation can be seen for the cases of landfast and multiyear ice of high ice concentrations R^2=0.36, RMS=0.065. Combining all aerial observations gives mean melt pond fraction RMS equal to 0.22.

3.3.2 Cloud screening for in situ and ship cruise validation

As the aerial validation has been performed on cloud free data, the problem of cloud clearing did not arise. For in situ and ship cruise data, cloud contamination may increase the uncertainty of the satellite retrieved values and in these cases this problem has to be addressed additionally. With the gridded product, the unscreened cloud edges and partly screened out clouds are cut out with the criterion for minimum valid data pixels allowed within one grid cell. For the swath data, such criterion is not applied and the existing cloud filtering proved to be not sufficient for a quality validation. Therefore, an additional spatial dynamic filter was introduced for ship cruise and in situ data. An example is shown in Figure 15.

The dynamic spatial filter consists of dividing the swath into boxes of 10x10 pixels with all the surface and cloud screening criteria applied except the oxygen A filter (Eq. 5 in Zege et al. (2015)); due to MERIS bands specifics, all these filters are imperfect and are subject to misclassifying certain types of clouds (e.g. thin clouds and ice clouds) as ice and snow. Then, within a given box, the oxygen A filter is applied. If this additional oxygen A filter screened out some additional pixels, then the box is potentially cloudy and the imperfect cloud filters surely left some unscreened clouds. Such a box is discarded completely. If the additional oxygen A filter (which is more sensitive to high and thick low clouds than the other applied cloud filters, so in the case of clouds it would screen out more pixels than the other filters) did not screen out any additional pixels, the scene is either uniformly filled with just clouds to which none of the filter are sensitive (improbable) or it is a cloud free scene. The boxes where this happens are kept and used for validation.

This method proved to be successful for the case studies on single swaths which do not undergo gridding with a threshold on the minimum allowed amount of cloud free pixels which helps to screen out cloud edges or partly screened clouds. For our MERIS gridded products, the gridding procedure tends to introduce a similar cloud screening effect as the above mentioned filter. High thin clouds, however, may still be present within both swath data and gridded products. The consequences are discussed in the Section 3.1.

3.3.3 Ship cruise validation

The visual estimations of various sea ice parameters, including MPF during the ship cruises differ in accuracy from aerial measurements, transect measurements, or visual estimations during in situ campaigns which are dedicated to such measurements. As opposed to the in situ campaign, hourly bridge observations are performed by many observers with different estimation experience and skill, which introduces additional noise to the observed value. The two studied cruises – The Healy-Oden Transarctic Expedition (HOTRAX), 19 August – 27 September 2005 (Perovich et al., 2009), and RV Polarstern cruise ARK-XXVI-3 (TransArc2011), 04 August 2011 – 6 October 2011 (Nicolaus et al., 2012), - both travelled across the Arctic Ocean at the end of melt season, August-September. The occurrence of frozen over, snow covered or entirely melted through melt ponds was therefore high. The ice observations during both cruises have been performed within the Antarctic Sea Ice Processes and Climate (ASPeCt) protocol (http://aspect.antarctica.gov.au/). The specifics of ASPeCt ice watch protocol lead to lack of fields for detailed description of the state of melt ponds. During TransArc2011 such details were sometimes (but not always) mentioned in the field for comments, and for HOTRAX cruise such information was not available at all. Where available these details are helpful for the validation of the MPD algorithm. Spectral reflectance of frozen and snow covered ponds can be represented as a linear mixture of dark pond and sea ice within the MERIS spectral range, and melted through ponds have the spectral behaviour of open water. Both surface types are no longer melt ponds in the original sense of the word and have to be excluded from the retrieved MPF for energy budget or climate modelling applications. As the MPD algorithm utilizes the difference in spectral behaviour of melt ponds, open water and sea ice, it will retrieve the true fraction of open melt ponds with sea ice underneath the meltwater. In case of melted through or frozen over ponds documented as melt ponds in the ship based observations, a discrepancy between the ship cruise data and the MPF retrieval will occur. This is illustrated for the case of the frozen snow covered melt ponds in Figure 16. The MPD will continue to retrieve some MPF also in case of frozen ponds as long as their albedo is lower than the albedo of surrounding sea ice. Typically a few centimeters of snow is already enough to even out this albedo difference, but horizontal snow redistribution due to winds can prolong the period of apparent pond presence

according to the MPD retrieval. This explains the positive MPF bias in September (after the melt season) in Figure 3.

Within this work, we apply the MPD algorithm without limitations other than cloud screening (original as described by Zege et al. (2015), and dynamic spatial filter described in Sect. 3.3.2) to illustrate the effect of the above mentioned underestimation. In cases not dedicated to the study of the algorithm accuracy, it is recommended to use the MPD MPF product in combination with the reanalysis air surface temperature to apply the algorithm only when the melt ponds are not frozen over. Otherwise the (supposedly low) MPF value is ambiguous and could indicate both low MPF of open ponds or high MPF of frozen ponds.

Both cruises TransArc2011 (Figure 17) and HOTRAX 2005 (Figure 18) had only several days of cloud free collocations. The available swath data and the hourly ship observations have been compared point by point without temporal averaging. The only averaging was the 15km spatially of the satellite data around the ship location. For both cruises, information on ice concentration was available from bridge observations and the ship MP values have been corrected for ice concentration to give the pond fraction relative to the visible area and not to the area of sea ice. For the TransArc2011 cruise, information on MYI and FYI ice concentration was available with corresponding MPFs. The total MPF was calculated using the linear mix of these values. However, the resulting cloud free collocations feature mostly FYI cases. For the HOTRAX 2005, such information was not available and only total ice concentrations were used. The correlation between the satellite value and observed value: mean R^2=0.044, mean RMS=0.16. The low correlation might be caused by the documentation of varying accuracy within the ASPeCt protocol.

3.3.4 In situ validation

The in situ validation has been performed on the swath data using the three available datasets: transect measurements on the FI just north of Barrow, AK, approximately 1km offshore from Niksiuraq in the Chukchi sea, near 71°22′ N, 156°33′ W throughout June 2009 (Polashenski et al., 2012), 100m transect and visual estimations on the 3x3 km area of landfast FYI approximately 80 km northwest of Resolute Bay, Nunavut, 75°14′ N, 97°09′ W, between June 18 and July 10, 2002 as part of the Collaborative Interdisciplinary Crysophere Experiment (C-ICE) 2002 project (Scharien and Yackel, 2005), and 200m transect fractions

on landfast FYI also in the vicinity of Resolute Bay, Nunavut, 74°44′ N, 95°06′ W, between June 26 and July 11, 2006 (Sect. 3.2.1).

During C-ICE 2002 visual estimates of MPF fraction were made on a homogeneous and relatively smooth zone of FI in the Canadian Arctic Archipelago approximately 80 km northwest of Resolute Bay, Nunavut between June 18, 2002 and July 08, 2002 (Scharien and Yackel, 2005). Visual estimates were supported by occasional 100 m transect measurements taken at 0.5 m intervals to characterize surface feature types (melt pond or ice) and pond depths, as well as timelapse photos taken from a tower based camera mounted at 6 m height. From these data a nominal 0.1 MPF estimation error was ascribed to the visual estimates. For days where transect measurements were available, the daily average of W-E and N-S transects was used instead of visual estimates.

For the remaining two datasets, the transect measurements of MPFs were used as provided.

The datasets feature uniform FI and at times of extremely high pond fractions and the following drainage events. As the campaigns were performed on the FI, no correction for the ice concentration was needed. As in case of ship cruises, the average MPF 15km around each in situ point was taken. The same cloud filtering has been applied (original as described by Zege et al. (2015), and dynamic spatial filter described in Sect. 3.3.2). The total amount of cloud free collocated points is N=47, total RMS = 14%, total R^2=0.52. The correlation plot for the two datasets is shown in Figure 18.

4 Conclusions

Melt ponds on sea ice affect the radiative properties of the ice cover and its heat and mass balance. In order to assess the change of the energy budget in the region (e.g. with GCM), among other sea ice and melt pond properties, the sea ice reflective properties and the amount of melt ponds on sea ice have to be known. This work has validated a retrieval of MPF and broadband sea ice albedo from MERIS data (Zege et al., 2015) against aerial, in situ and ship-based observations.

The cloud screening presented in Zege et al. (2015) has been compared to the AATSR cloud screening presented in Istomina et al. (2010) for swath data of both sensors collocated to AATSR swath, for the whole summer 2009. The comparison (Figure 3) shows that

unscreened clouds are seen as melt ponds before melt onset and as less melt ponds during melt evolution; the effect of unscreened clouds is not constant and depends on the true surface pond fraction. Unscreened clouds tend to smooth out the melt pond fraction values towards a mean value of about 0.15. As can be seen from the figure, this smoothing effect is most prominent in the beginning of the season and during the melt maximum, and is the smallest in June.

The albedo data from from spaceborne and airborne observations have been compared and showed high correlation when there is no ice drift (Figure 5, Figure 7). Same comparison for MPF highly depends on the ice conditions and melt stage: for FI and MYI in the beginning of melt the correlation is high (Figure 11, Figure 12, Figure 19), for separate FYI floes the correlation is worse maybe due to ice drift (Figure 13, Figure 14). The comparison of ship cruise data to satellite retrieved MPF for FYI and MYI at the end of the melt season shows strong underestimation of satellite retrieval. This might be connected to frozen over ponds undocumented in the ASPeCt observations (Figure 17, Figure 18). At the same time, comparison to ship observations show that the MPD retrieval shows ambiguity of the retrieved MPF: low retrieved MPF could indicate low MPF of open ponds or high MPF of frozen ponds. It is planned to resolve this ambiguity in the future versions of the algorithm by introducing a decision tree based on the air temperature as a measure of surface energy balance to determine whether ponds are frozen over or not.

The presented melt pond fraction and sea ice albedo retrieval can be applied to other radiometers with sufficient amount of channels in the VIS and NIR regions of spectrum, e.g. VIIRS onboard Suomi NPP and OLCI onboard the Sentinel-3 ESA mission (planned launch late 2015). Thus the continuity of the MPF and sea ice albedo dataset can be achieved, which is important for the dataset use as input to GCM and for studies of MPF and albedo dynamics in the context of global change and Arctic amplification.

The case studies, time sequence analysis and trends of MPF and sea ice albedo are presented in the companion paper (Istomina et al., 2015).

Acknowledgements

The authors express gratitude to Dr. Stefan Hendricks for providing photos of the hourly bridge observations of the TransArc 2011 cruise, to Dr. Daniel Steinhage for providing photos

taken with a downward-looking camera during the aircraft campaign NOGRAM-2 2011, to the C-ICE 2002 participants, J. Yackel and the Cryosphere Climate Research Group, Department of Geography, University of Calgary. The Centre for Earth Observation Science at the University of Manitoba and the Polar Continental Shelf Project are gratefully recognized for their logistic and financial support.

The authors are grateful to the two anonymous reviewers and the editor Dr. H. Eicken for their effort and valuable comments on the manuscript.

This work has been funded as a part of EU project SIDARUS.

References

Bannehr, L. and Schwiesow, R.: A Technique to Account for the Misalignment of Pyranometers Installed on Aircraft, J. Atmos. Ocean. Technol., 10(5), 774–777, doi:10.1175/1520-0426(1993)010<0774:ATTAFT>2.0.CO;2, 1993.

Barber, D. G. and Yackel, J.: The physical, radiative and microwave scattering characteristics of melt ponds on Arctic landfast sea ice, Int. J. Remote Sens., 20(10), 2069–2090, 1999.

Birnbaum, G., Dierking, W., Hartmann, J., Lüpkes, C., Ehrlich, A., Garbrecht, T. and Sellmann, M.: The Campaign MELTEX with Research Aircraft "POLAR 5" in the Arctic in 2008, Berichte zur Polar- und Meeresforschung/Reports Polar Mar. Res., 593, 3–85, 2009.

Bricaud, A., Morel, A. and Prieur, L.: Absorption by dissolved organic matter of the sea Domains, (yellow substance) in the UV and visible, Limnol. Ocean.,26(1), 43–53, 1981.

Curry, J. A., Schramm, J. L. and Ebert, E. E.: Sea-ice albedo climate feedback mechanism, J. Clim., 8(2), 240–247, 1995.Eicken, H., Grenfell, T. C., Perovich, D. K., Richter-Menge, J. A. and Frey, K.: Hydraulic controls of summer Arctic pack ice albedo, J. Geophys. Res. C Ocean., 109(8), C08007, doi:10.1029/2003JC001989, 2004.

Geldsetzer, T., Scharien, R. K., Yackel, J. J., Cheng, B. and Else, B. G. T.: Multipolarization SAR for operational sea ice monitoring, Technical Report for POL-ICE 2006 2006-12-11., 2006.

Gonzalez, R. C. and Woods, R. E.: Digital Image Processing, Second Edition, Prentice Hall Inc., 2002.

Grenfell, T. C. and Perovich, D. K.: Seasonal and spatial evolution of albedo in a snow-ice-land-ocean environment, J. Geophys. Res., 109(C1), C01001, doi:10.1029/2003JC001866, 2004.

Hanesiak, J. M., Barber, D. G., De Abreu, R. A. and Yackel, J. J.: Local and regional albedo observations of arctic first-year sea ice during melt ponding, J. Geophys. Res., 106(C1), 1005, 2001.

Istomina, L. G., Heygster, G., Huntemann, M., Marks, H., Zege, E. P., Malinka, A. V., Prikhach, A. S. and Katsev, I. L.: The melt pond fraction and spectral sea ice albedo retrieval from MERIS data II: case studies and trends of sea ice albedo and melt pond fraction in the Arctic for years 2002-2011, Cryosph., 2015.

Istomina, L. G., von Hoyningen-Huene, W., Kokhanovsky, A. A. and Burrows, J. P.: The detection of cloud-free snow-covered areas using AATSR measurements, Atmos. Meas. Tech., 3(4), 1005–1017, doi:10.5194/amt-3-1005-2010, 2010.

Istomina, L., Nicolaus, M. and Perovich, D.: Spectral albedo of sea ice and melt ponds measured during POLARSTERN cruise ARK XXII/3 (IceArc) in 2012. PANGAEA Dataset., doi:10.1594/ PANGAEA.815111, 2013.

Jensen, J.: Introductory digital image processing: a remote sensing perspective, Third Edition, Prentice Hall Inc., 2008.

Kokhanovsky, A. a., Budak, V. P., Cornet, C., Duan, M., Emde, C., Katsev, I. L., Klyukov, D. A., Korkin, S. V., C-Labonnote, L., Mayer, B., Min, Q., Nakajima, T., Ota, Y., Prikhach, A. S., Rozanov, V. V., Yokota, T. and Zege, E. P.: Benchmark results in vector atmospheric radiative transfer, J. Quant. Spectrosc. Radiat. Transf., 111(12-13), 1931–1946, doi:10.1016/j.jqsrt.2010.03.005, 2010.

Lampert, A., Maturilli, M., Ritter, C., Hoffmann, A., Stock, M., Herber, A., Birnbaum, G., Neuber, R., Dethloff, K., Orgis, T., Stone, R., Brauner, R., Kässbohrer, J., Haas, C., Makshtas, A., Sokolov, V. and Liu, P.: The Spring-Time Boundary Layer in the Central Arctic Observed during PAMARCMiP 2009, Atmosphere (Basel)., 3(4), 320–351, doi:10.3390/atmos3030320, 2012.

Lehmann, P.: Geophysikalische Messungen für Nordostgrönland, Scientific report, Bremerhaven., 2012.

Nicolaus, M., Katlein, C., Maslanik, J. A. and Hendricks, S.: Sea ice conditions during the POLARSTERN cruise ARK-XXVI/3 (TransArc) in 2011, PANGAEA Dataset., doi:10.1594/PANGAEA.803312, 2012.

Perovich, D. K.: The Optical Properties of Sea Ice, Hanover (NH, USA) US Army Cold Reg. Res. Eng. Lab. Rep. 96-1. www.dtic.mil/cgi-bin/ GetTRDoc?AD=ADA310586, (May), 1996.

Perovich, D. K., Grenfell, T. C., Light, B., Elder, B. C., Harbeck, J., Polashenski, C., Tucker, W. B. and Stelmach, C.: Transpolar observations of the morphological properties of Arctic sea ice, J. Geophys. Res. C Ocean., 114(1), C00A04, doi:10.1029/2008JC004892, 2009.

Polashenski, C.: Attributing Change and Understanding Melt Ponds on a Seasonal Ice Cover, 181 pp., Darthmouth College, Hanover, New Hampshire., 2011.

Polashenski, C., Perovich, D. and Courville, Z.: The mechanisms of sea ice melt pond formation and evolution, J. Geophys. Res., 117(C1), C01001, doi:10.1029/2011JC007231, 2012.

Press, W., Teukolsky, S., Vetterling, W. and Flannery, B.: Numerical Recipes: The Art of Scientific Computing, Cambridge University Press., 1987.

Rösel, A., Kaleschke, L. and Birnbaum, G.: Melt ponds on Arctic sea ice determined from MODIS satellite data using an artificial neural network, Cryosph., 6(2), 431–446, doi:10.5194/tc-6-431-2012, 2012.

Scharien, R. K. and Yackel, J. J.: Analysis of surface roughness and morphology of first-year sea ice melt ponds: Implications for microwave scattering, IEEE Trans. Geosci. Remote Sens., 43(12), 2927–2939, 2005.

Scharien, R. K., Yackel, J. J., Barber, D. G., Asplin, M., Gupta, M. and Isleifson, D.: Geophysical controls on C band polarimetric backscatter from melt pond covered Arctic first-year sea ice: Assessment using high-resolution scatterometry, J. Geophys. Res. Ocean., 117(C9), n/a–n/a, doi:10.1029/2011JC007353, 2012.

Schlundt, C., Kokhanovsky, A. A., von Hoyningen-Huene, W., Dinter, T., Istomina, L. and Burrows, J. P.: Synergetic cloud fraction determination for SCIAMACHY using MERIS, Atmos. Meas. Tech., 4(2), 319–337, doi:10.5194/amt-4-319-2011, 2011.

Schröder, D., Feltham, D. L., Flocco, D. and Tsamados, M.: September Arctic sea-ice minimum predicted by spring melt-pond fraction, 4(May), 353–357, doi:10.1038/NCLIMATE2203, 2014.

Schwarz, P.: Quantitative characterisation of sea ice melt stages in the Arctic by means of airborne photographs, 114 pp., University of Trier., 2013.

Shindell, D. and Faluvegi, G.: Climate response to regional radiative forcing during the twentieth century, Nat. Geosci., 2(4), 294–300, doi:10.1038/ngeo473, 2009.

Tschudi, M. A., Maslanik, J. A. and Perovich, D. K.: Derivation of melt pond coverage on Arctic sea ice using MODIS observations, Remote Sens. Environ., 112(5), 2605–2614, doi:10.1016/j.rse.2007.12.009, 2008.

Tynes, H. H., Kattawar, G. W., Zege, E. P., Katsev, I. L., Prikhach, A. S. and Chaikovskaya, L. I.: Monte Carlo and Multicomponent Approximation Methods for Vector Radiative Transfer by use of Effective Mueller Matrix Calculations, Appl. Opt., 40(3), 400, doi:10.1364/AO.40.000400, 2001.

Warren, S. G. and Brandt, R. E.: Optical constants of ice from the ultraviolet to the microwave: A revised compilation, J. Geophys. Res. D Atmos., 113(14), D14220, doi:10.1029/2007JD009744, 2008.

Yackel, J., Barber, D. G. and Hanesiak, J. M.: Melt ponds on sea ice in the Canadian Archipelago: 1. Variability in morphological and radiative properties, J. Geophys. Res., 105(C9), 22049–22060 doi: 10.1029/2000JC900075, 2000. Zege, E. P., Ivanov, A. P. and Katsev, I. L.: Image transfer through a scattering medium, Springer-Verlag, Heidelberg., 1991.

Zege, E. P., Malinka, A. V., Katsev, I. L., Prikhach, A. S., Heygster, G., Istomina, L. G., Birnbaum, G. and Schwarz, P.: Algorithm to retrieve the melt pond fraction and the spectral albedo of Arctic summer ice from satellite data, Remote Sens. Environ., 163, 153-164, doi:10.1016/j.rse.2015.03.012, 2015.

1 Table 1. Datasets used for validation of the MPD algorithm

Campaign and year	Method	Ref.
Barrow 2009	In situ field campaign, fractions along a 200m transect	(Polashenski, 2011)
MELTEX 2008	Airborne measurements, supervised classification algorithm applied to geolocated quality assured aerial images	(Birnbaum et al., 2009; Schwarz, 2013)
NOGRAM-2 2011	Airborne measurements, supervised classification algorithm applied to geolocated quality assured aerial images	(Lehmann, 2012; Schwarz, 2013)
C-ICE 2002	In situ field campaign, visual estimation and fractions along 100m transects	(Scharien and Yackel, 2005)
HOTRAX 2005	Ship cruise, hourly bridge observations, visual estimation	(Perovich et al., 2009)
TransArc 2011	Ship cruise, hourly bridge observations, visual estimation	(Nicolaus et al., 2012)
POL-ICE 2006	In situ field campaign, fractions along a 200m transect	(R. Scharien, Sect. 3.2.1)

2

Table 2. Transect measurements of surface type fractions in the Canadian Arctic, POL-ICE 2006, where the relative surface type fractions are as follows: f_1 is the snow/bare ice, f_2 – melt pond, f_3 – mixed cover, f_4 – overfrozen melt pond.

id	date_ut	time_ut	loc_y	loc_x	n	f_1	f_2	f_3	f_4
1	26-Jun-2006	15:00	74.73324	-95.10583	383	0.37	0.31	0.32	0.00
2	27-Jun-2006	0:00	74.732	-95.10324	400	0.23	0.41	0.36	0.00
3	28-Jun-2006	0:00	74.73164	-95.14458	395	0.21	0.57	0.22	0.00
4	28-Jun-2006	18:30	74.73079	-95.14778	401	0.24	0.54	0.22	0.00
5	2-Jul-2006	15:00	74.73015	-95.16151	398	0.35	0.26	0.39	0.00
6	4-Jul-2006	17:30	74.73102	-95.15971	400	0.37	0.31	0.32	0.00
7	5-Jul-2006	14:45	74.7304	-95.17052	400	0.24	0.41	0.35	0.00
8	6-Jul-2006	3:00	74.73097	-95.1729	400	0.22	0.41	0.38	0.00
9	6-Jul-2006	17:00	74.7309	-95.17329	400	0.31	0.30	0.40	0.00
10	9-Jul-2006	15:00	74.72987	-95.17271	400	0.38	0.06	0.38	0.19
11	10-Jul-2006	0:30	74.7301	-95.17448	400	0.30	0.09	0.61	0.00
12	11-Jul-2006	16:45	74.72998	-95.16605	400	0.33	0.22	0.46	0.00

Table 3. Integrated (320-950nm) albedo for various surface types and total obtained from transect radiance measurements in Canadian Arctic, POL-ICE 2006, versus corresponding retrieved broadband (400-900nm) albedo averaged within 5 km around the location. n is the amount of measurements, f is the surface type fraction, α is the integrated albedo.

	SNOW/BARE ICE				**MIXED**				**POND**				**RESULT**
id	n	f	avg α	std α	n	f	avg α	std α	n	f	avg α	std α	**Total α** /retrieved
2	83	0.21	0.51	0.07	86	0.22	0.31	0.05	226	0.57	0.24	0.03	**0.31**/N/A
3	94	0.24	0.62	0.06	89	0.22	0.40	0.13	217	0.54	0.23	0.02	**0.36**/0.47
6	149	0.37	0.57	0.05	126	0.32	0.33	0.10	125	0.31	0.22	0.03	**0.38**/N/A
7	97	0.24	0.54	0.05	140	0.35	0.29	0.10	163	0.41	0.21	0.02	**0.32**/0.40
9	122	0.31	0.58	0.04	158	0.40	0.32	0.11	120	0.30	0.20	0.01	**0.36**/0.58
10	150	0.38	0.68	0.04	152	0.38	0.38	0.12	23	0.06	0.20	0.01	**0.46**/0.48
11	119	0.30	0.56	0.04	244	0.61	0.30	0.11	37	0.09	0.18	0.01	**0.37**/N/A
12	132	0.33	0.71	0.07	182	0.46	0.33	0.16	86	0.22	0.20	0.02	**0.43**/N/A
Combined			**0.60**	**0.08**			**0.33**	**0.12**			**0.21**	**0.03**	

Table 4. UTC time of aerial measurements (mpf and alb) and satellite overflights (sat) for each day of available aerial measurements of MELTEX 2008 and NOGRAM 2011. Cases with large time difference (greater than 1.5^{h}) between satellite and field measurements are shown in red.

Date	26.05.2008	03.06.2008	04.06.2008	06.06.2008	07.06.2008	21.07.2011
alb	20:45-21:48	17:00-19:46	19:14-23:24	no drift,	17:08-20:17	no drift,
mpf	20:55-22:55	16:59-17:53	19:14-22:03	FI	17:56-19:22	MYI
sat	20:46	19:54	21:02		21:08	

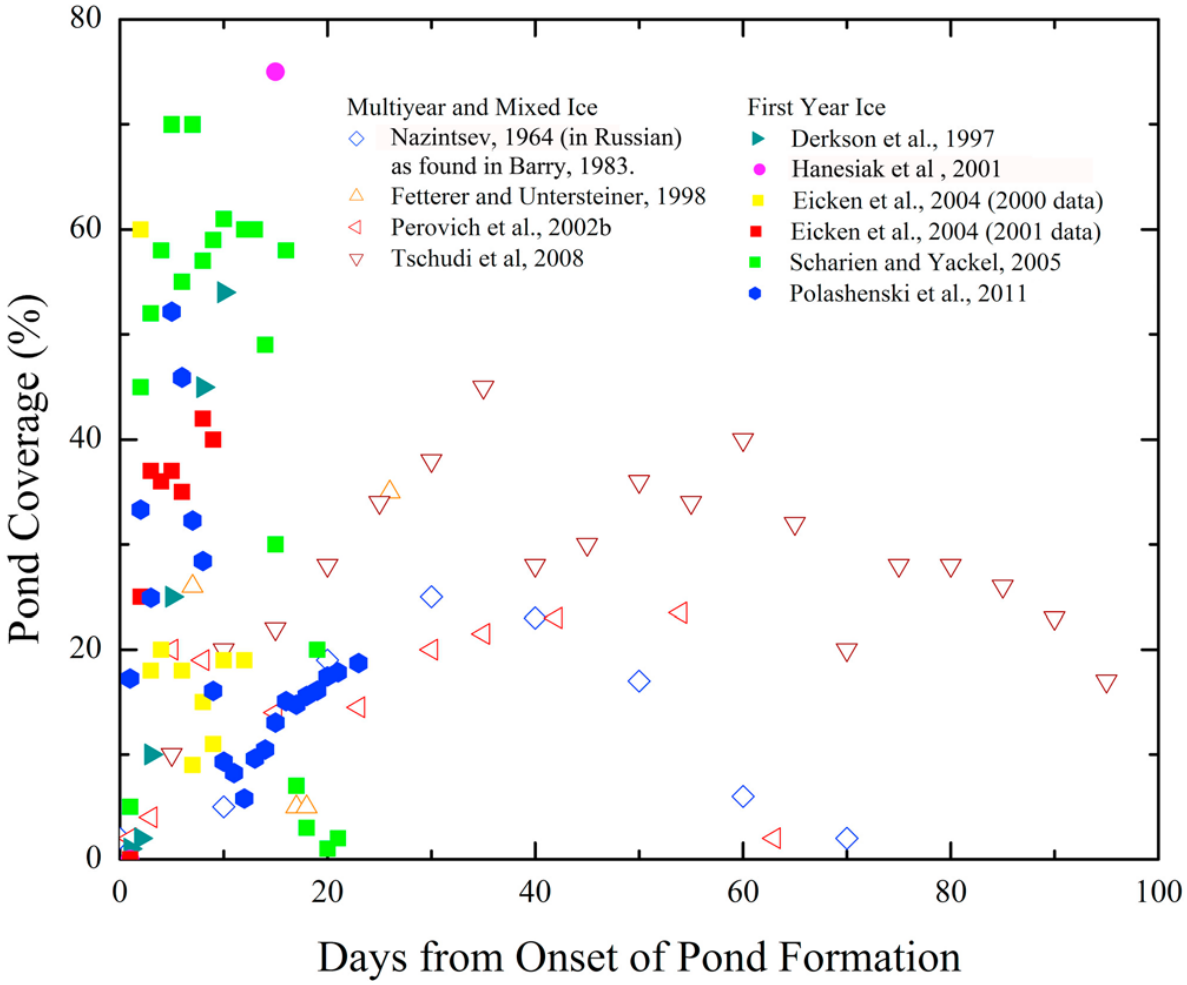

Figure 1. Pond coverage taken from various field campaigns (see legend) versus days from onset of ponding on first year ice (filled dots) and multiyear ice (empty dots). Melt onset proceeds rapidly to the MPF maximum on FYI with following pond drainage and moderate MPFs afterwards; on multiyear ice, the evolution of melt up to the melt maximum takes longer, the peak MPF value is lower and the MPF decrease is slower than that on FYI. Figure courtesy C. Polashenski.

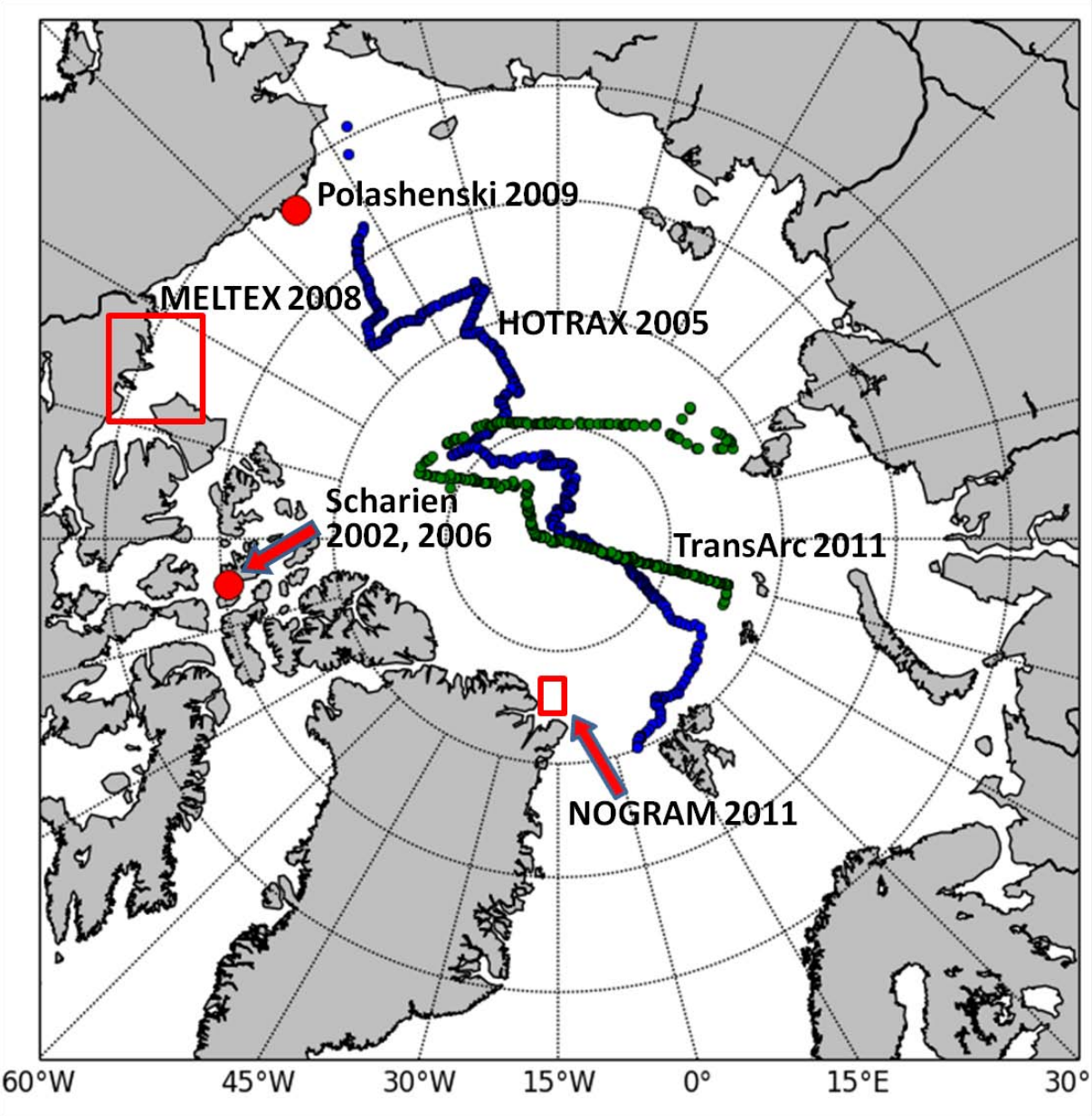

Figure 2. Schematic representation of the spatial distribution of the validation data. Red dots show the location of in situ field measurements; tracks – ship cruises, rectangles – approximate area of airborne measurements. The data includes FYI and MYI.

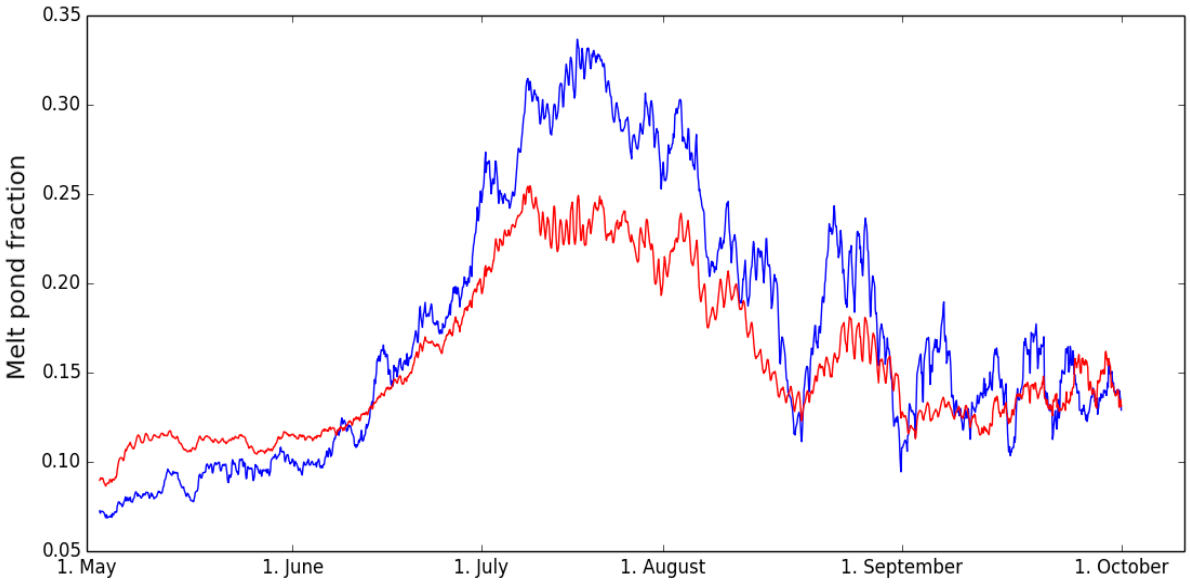

Figure 3. Swathwise comparison of the MERIS cloud mask used in the MPD retrieval to the AATSR cloud mask presented in (Istomina et al., 2010). The region covered is the Arctic Ocean to the north of 65°N (land masked out). All available swaths from May, 1, 2009 to September, 30, 2009 have been taken. Blue curve: MPF retrieved with MPD averaged in cloud free areas as seen by AATSR (reference or "perfect" cloud mask). Red curve: MPF retrieved with MPD averaged in cloud free areas as seen by MERIS (potentially cloud contaminated mask). The smoothing out effect of unscreened clouds is visible in the behavior of the red curve.

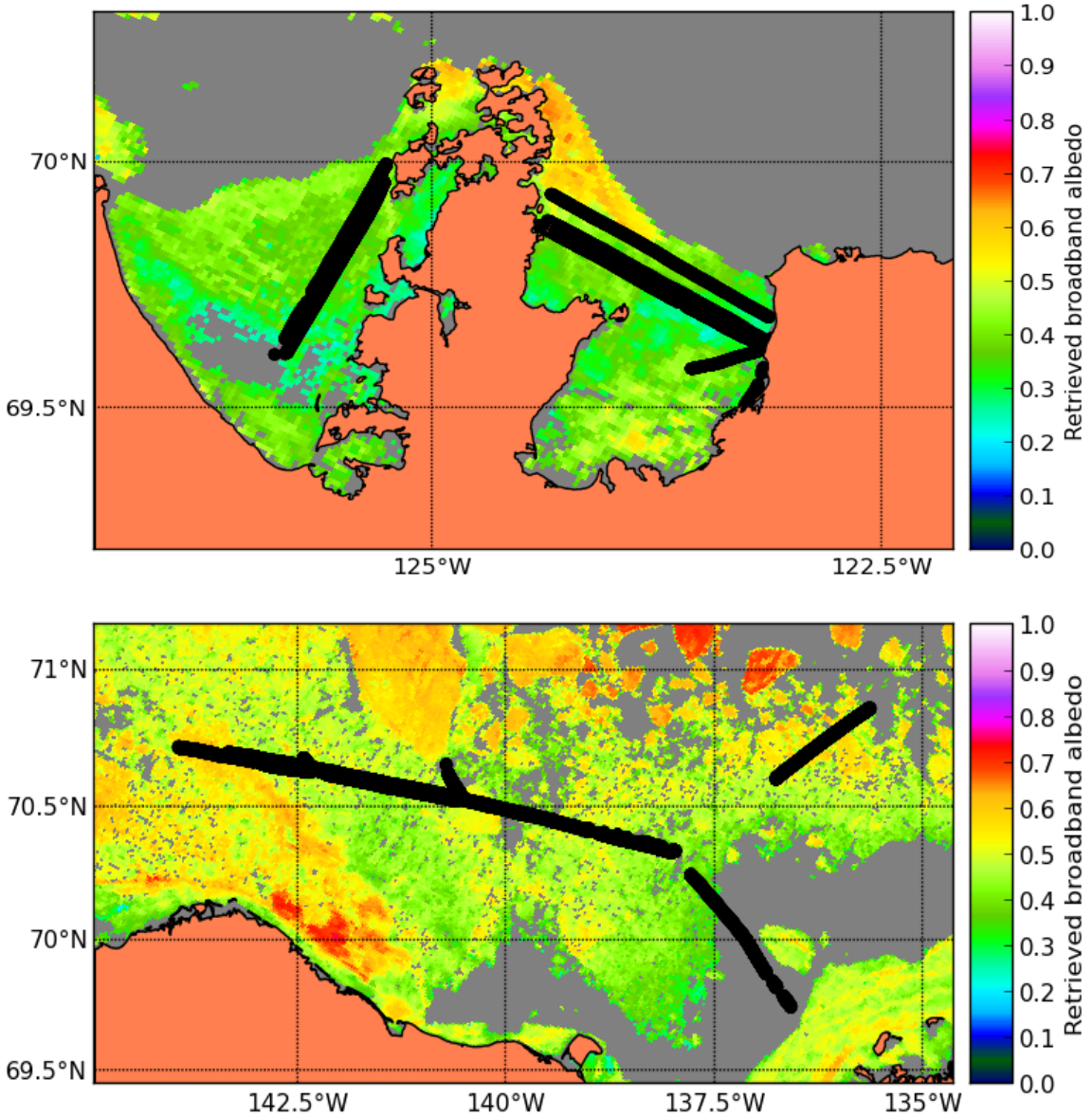

Figure 4. Examples of ice conditions present during MELTEX 2008 flights over landfast ice on June 06, 2008 (top panel) and over separate ice floes of various sizes on June 04, 2008 (bottom panel). The black tracks depict the flight tracks with albedo measurements. The color code illustrates the satellite retrieved broadband albedo. The background consists of the coral filled landmask and grey filled data gaps due to cloud contamination or surface type other than sea ice.

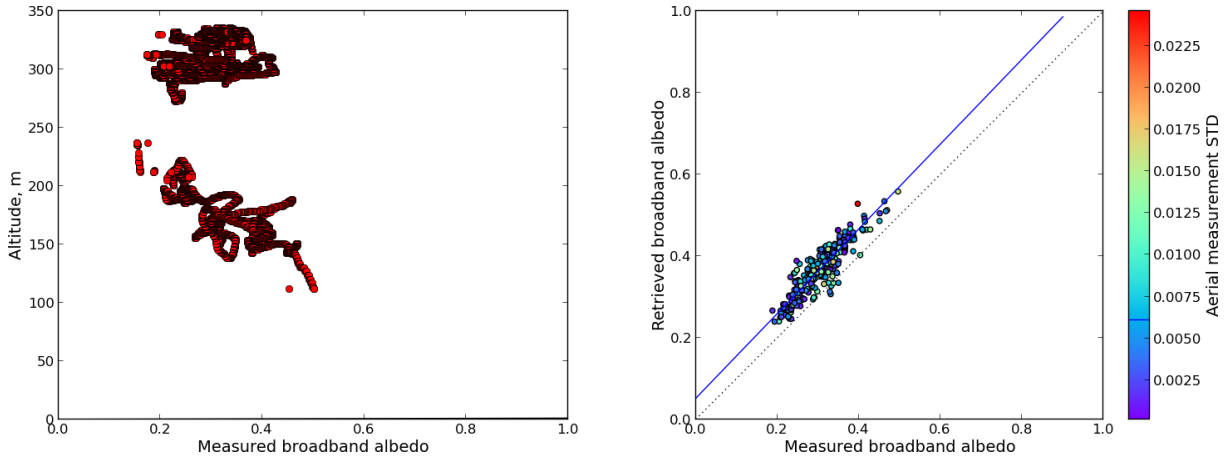

Figure 5. Altitude of the airborne broadband albedo measurements on June 06, 2008, MELTEX campaign (left). Correlation between retrieved broadband albedo from satellite data and measured broadband albedo over landfast ice (no drift) (flight track shown on the top panel Figure 3). STD is calculated from all collocated aerial measurements for a given satellite pixel. Only pixels with STD smaller than the mean STD are used. N = 169, R = 0.84, RMS=0.068.

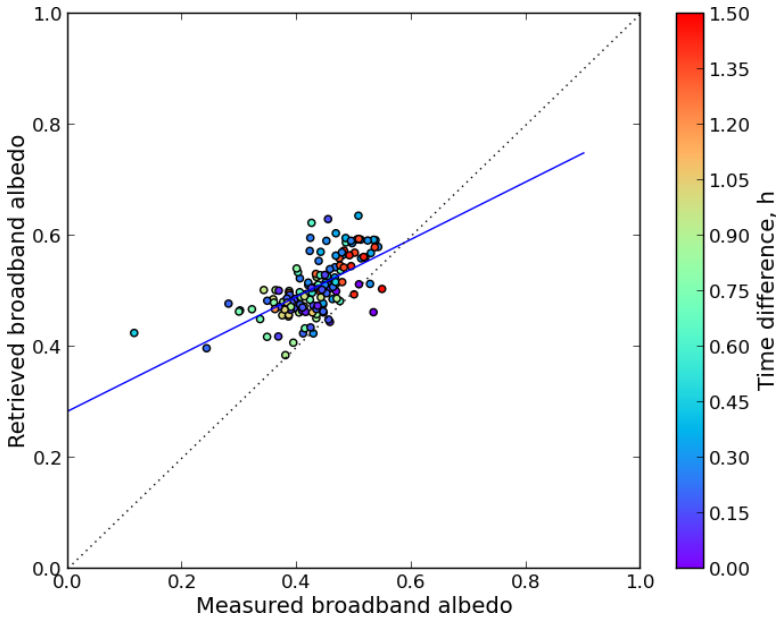

Figure 6. Correlation between broadband albedo retrieved from airborne measurements and from a satellite overflight, respectively, for the June 04, 2008, MELTEX campaign (bottom panel of Figure 3) with respect to time difference. N=147, R^2=0.39, RMS=0.089.

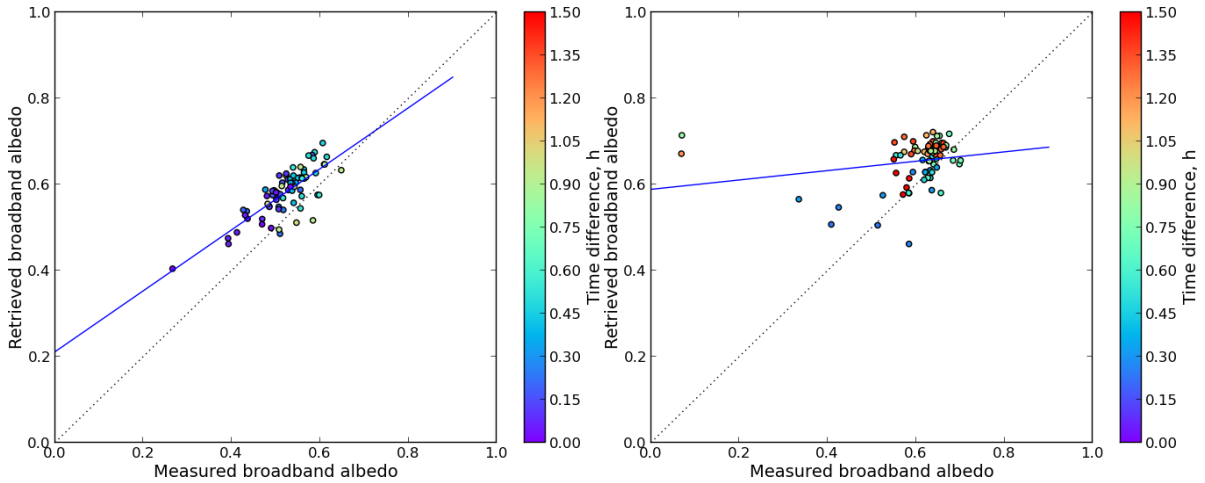

Figure 7. Correlation between broadband albedo retrieved from airborne measurements (MELTEX campaign) and from a satellite overflight, respectively, for the May 26, 2008 (left panel), N=73, R^2=0.61, RMS=0.07 and June 03, 2008, (right panel), N=78, R^2=0.05, RMS=0.121, with respect to time difference. The flight on June 03, 2008 features the greatest time difference to the satellite overflight, therefore most of the points have been discarded due to possible drift contamination.

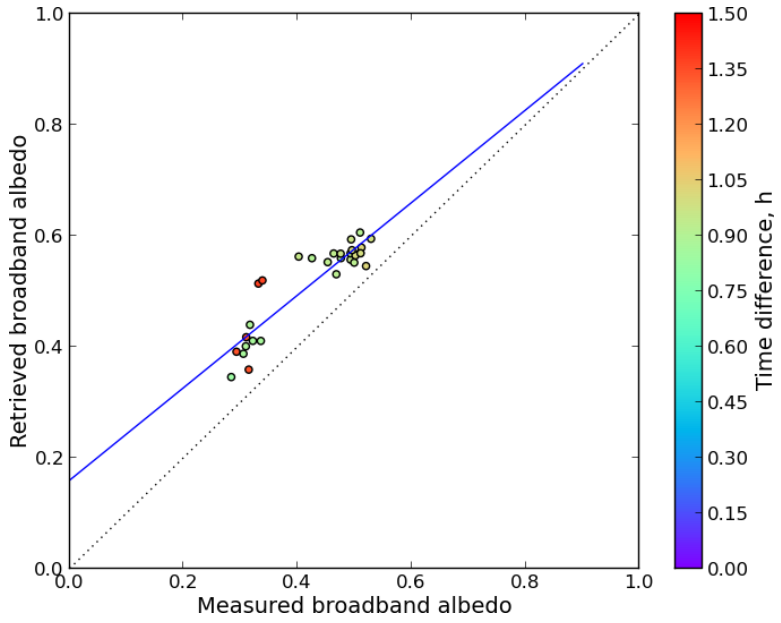

Figure 8. Correlation between broadband albedo retrieved from airborne measurements (MELTEX campaign) and from a satellite overflight, respectively, for the June 07, 2008, with respect to the time difference. N=30, R^2=0.82, RMS=0.096.

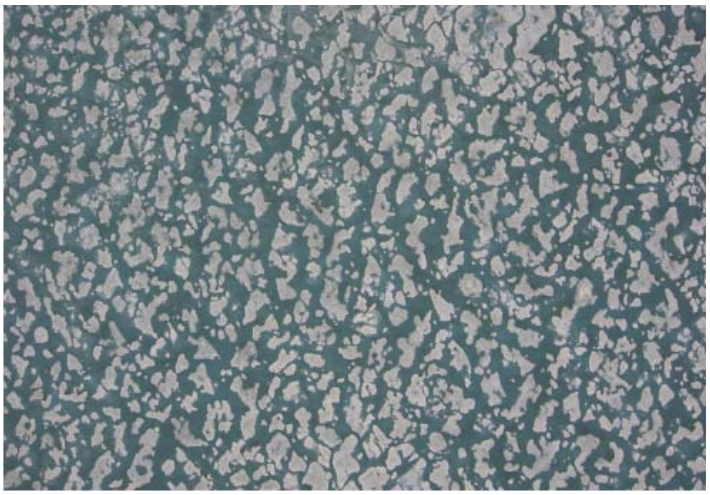

Figure 9. Example of aerial photo from MELTEX campaign in 2008, flight over landfast ice on June 04, 2008. The image width is approximately 400 m. Only quality assessed images were taken (see text for details).

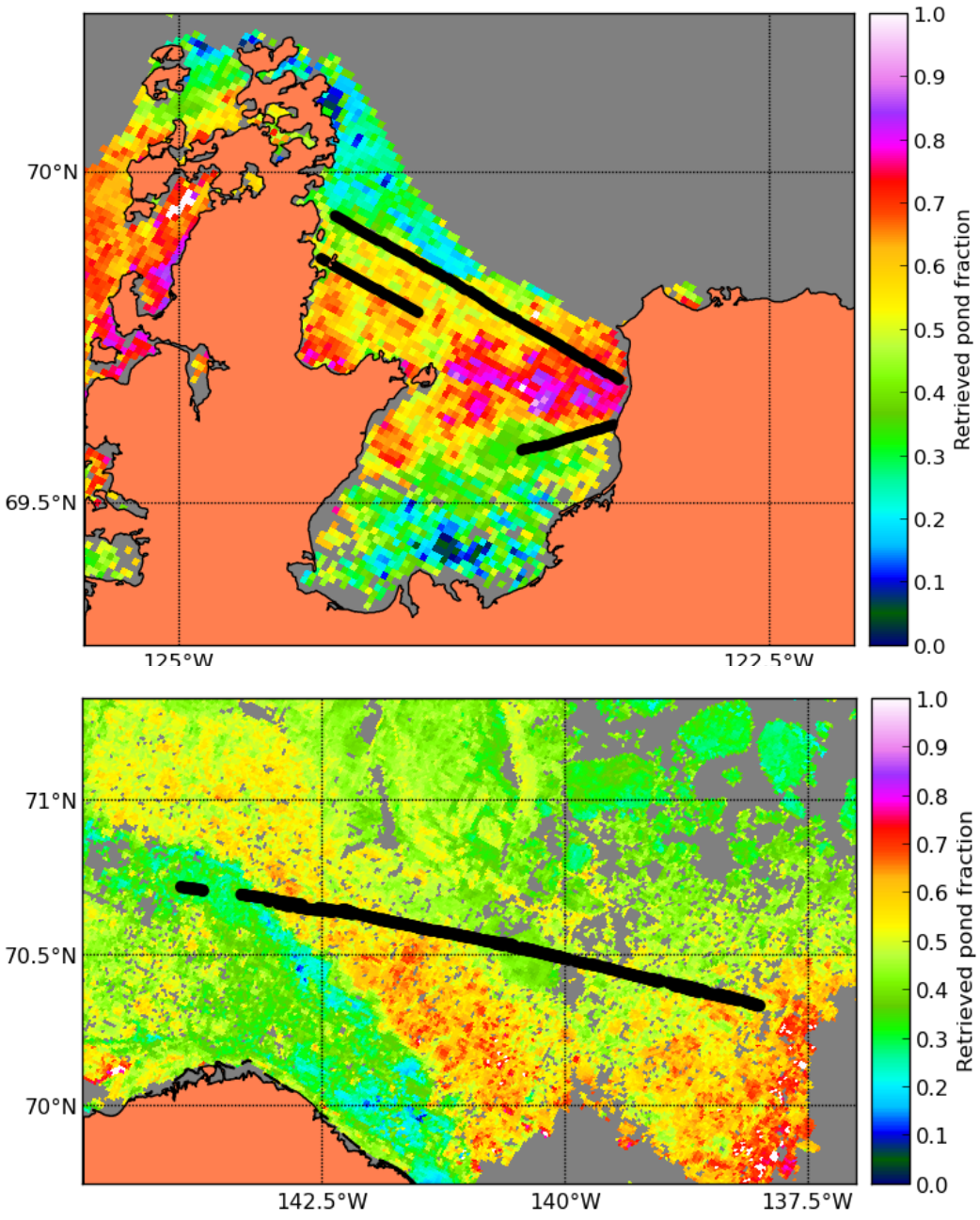

Figure 10. Examples of ice conditions present during MELTEX 2008 flights over landfast ice on June 06, 2008 (top panel) and over separate ice floes of various sizes on June 04, 2008 (bottom panel). Black dots: the flight track. The colored filled background: the satellite retrieved melt pond fraction. The background is the coral filled landmask and grey filled data gaps due to cloud contamination or surface type other than sea ice.

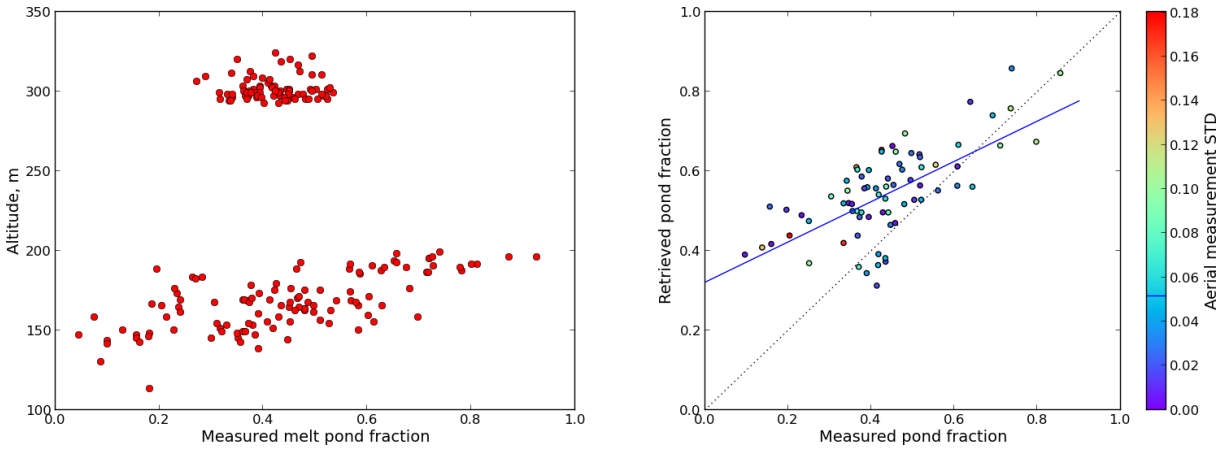

Figure 11. Altitude of the airborne melt pond measurements on June 06, 2008 (left). Correlation between retrieved melt pond fractions from satellite and airborne classified MPF over landfast ice with no drift (right), June 06, 2008 during MELTEX campaign. The flight track shown on the top panel Figure 9. N=48, R^2=0.36, RMS=0.154.

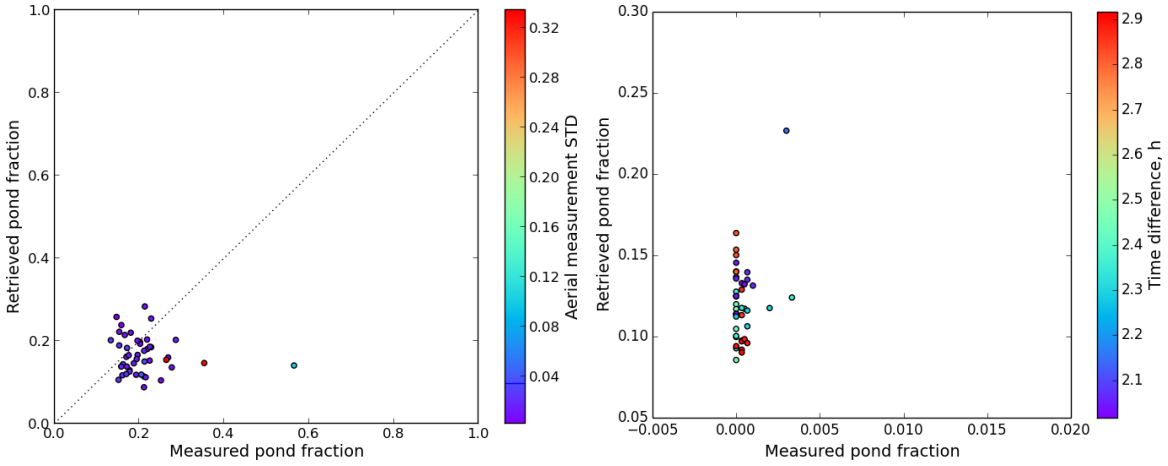

Figure 12. Correlation between retrieved melt pond fractions from satellite and airborne classified MP over MYI (no drift, ice pack), July 21, 2011, NOGRAM-2, 2011, campaign north of Greenland (left). N=40, R^2=0.004. RMS = 0.065 and over FYI, June 03, 2008, MELTEX 2008 (large floes but drift + large time difference) (right), N=44, R^2=0.13, RMS = 0.123. See Figure 2 for locations of the NOGRAM-2 and MELTEX campaigns.

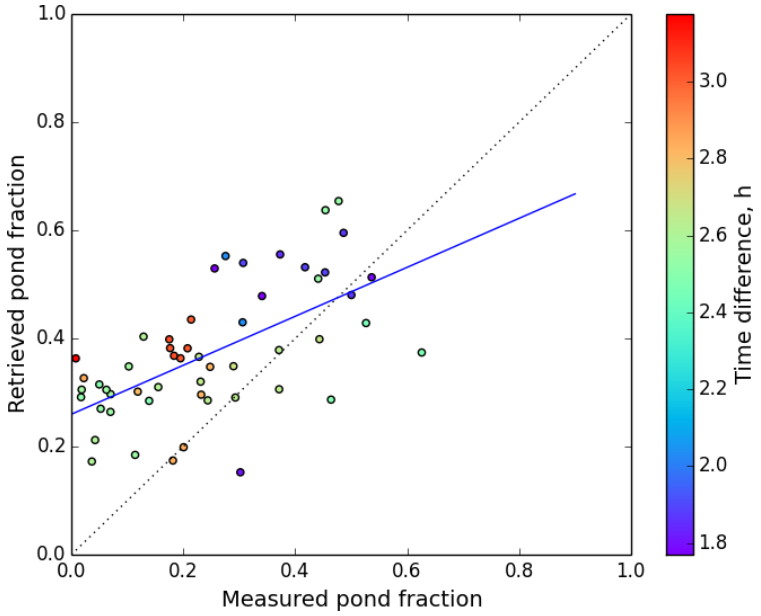

Figure 13. Correlation between retrieved melt pond fractions from satellite and airborne classified MP over FYI, possible drift, June 07, 2008, MELTEX2008, Beaufort Sea. This case features larger ice floes than flights on June 04 or May 26, 2008. N=53, R^2=0.37, RMS = 0.179.

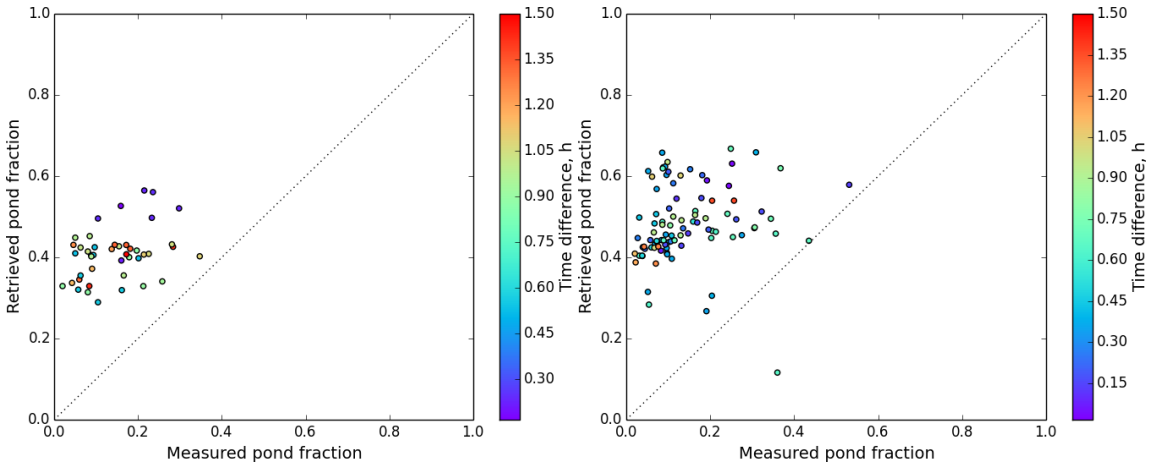

Figure 14. Retrieved melt pond fractions from satellite versus airborne classified MP over FYI, possible drift, May 26, 2008 (left panel), N=44, R^2=0.13, RMS=0.274, and June 04, 2008 (right panel, the flight track is shown in Figure 9, bottom panel), Beaufort Sea, N=93, R^2=0.02. RMS=0.361. Both cases feature brash ice with subpixel ice floes which are covered not with white ice, but with blue ice (sea ice without the scattering layer), which has spectral response similar to MP within the VIS and IR spectral range.

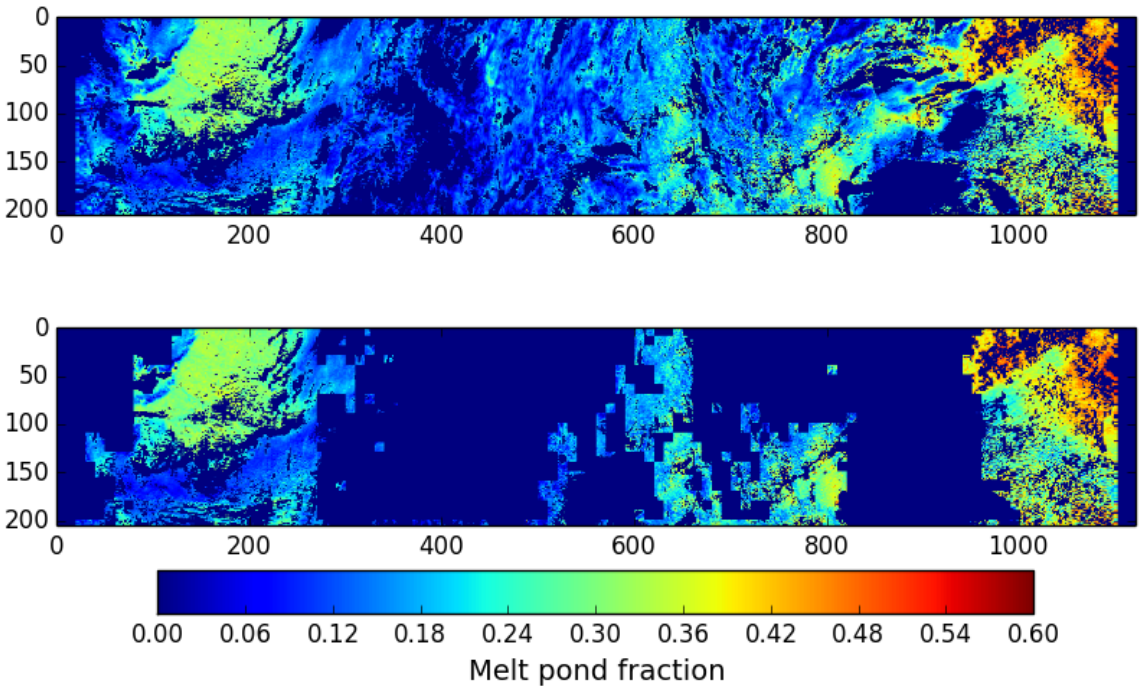

Figure 15. Example of a spatial dynamic cloud filtering for MERIS swath data: original swath subset with the cloud filters from (Zege et al., 2015) applied (top panel), same swath subset after applying the dynamic spatial filter (see text).

Figure 16. An example image made from the bridge of RV “Polarstern” during the TransArc 2011 (ARK XXVI3) on the 4th of September 2011 within the course of ASPeCt observations. The pond fraction estimated during the cruise is 0.5. The satellite retrieved pond fraction for such cases will be significantly smaller because of high albedo of frozen over snow covered ponds. Image source (Nicolaus et al., 2012).

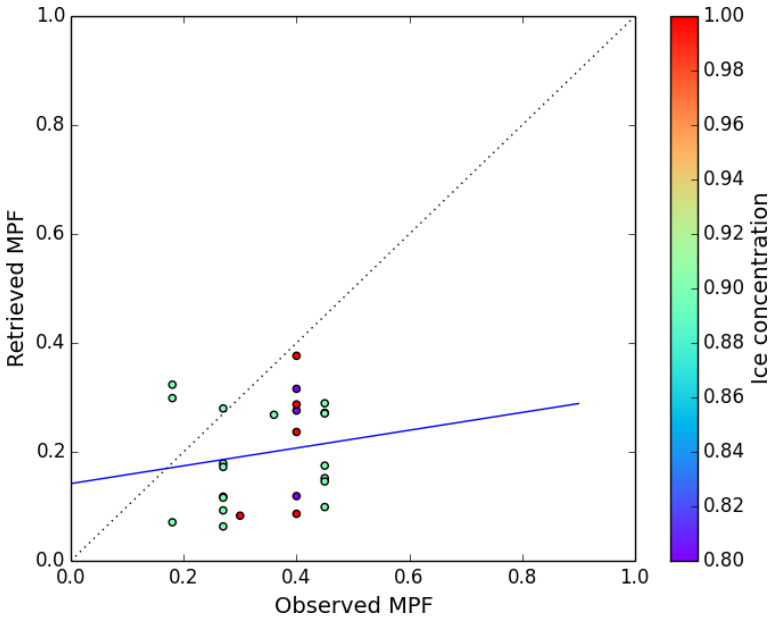

Figure 17. Retrieved MPF versus observed MPF from the hourly bridge observations during TransArc2011, 04 August 2011 – 6 October 2011. Swath data, no temporal averaging, 15km satellite average around the in situ point. All but one point is FYI. Corrected for ice concentration. Underestimation may be connected to undocumented presence of melted through or overfrozen ponds at the end of the melt season (see Figure 16). R^2=0.026, RMS=0.19, N=26.

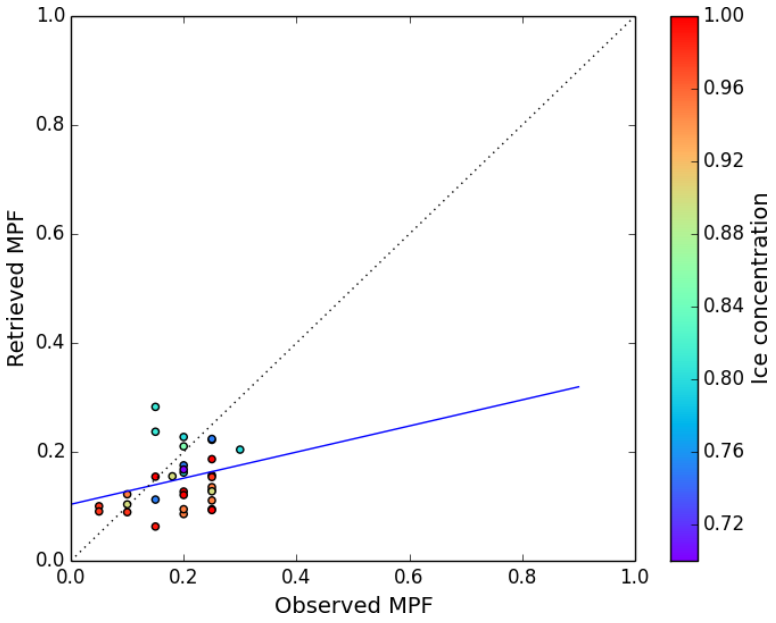

Figure 18. Retrieved MPF versus observed MPF from the hourly bridge observations during HOTRAX2005, 19 August – 27 September 2005. Swath data, no temporal averaging, 15km satellite average around the in situ point. No information on ice type. Corrected for ice concentration. Underestimation may be connected to undocumented presence of melted through or frozen over ponds at the end of the melt season. R^2=0.067, RMS=0.084, N=32.

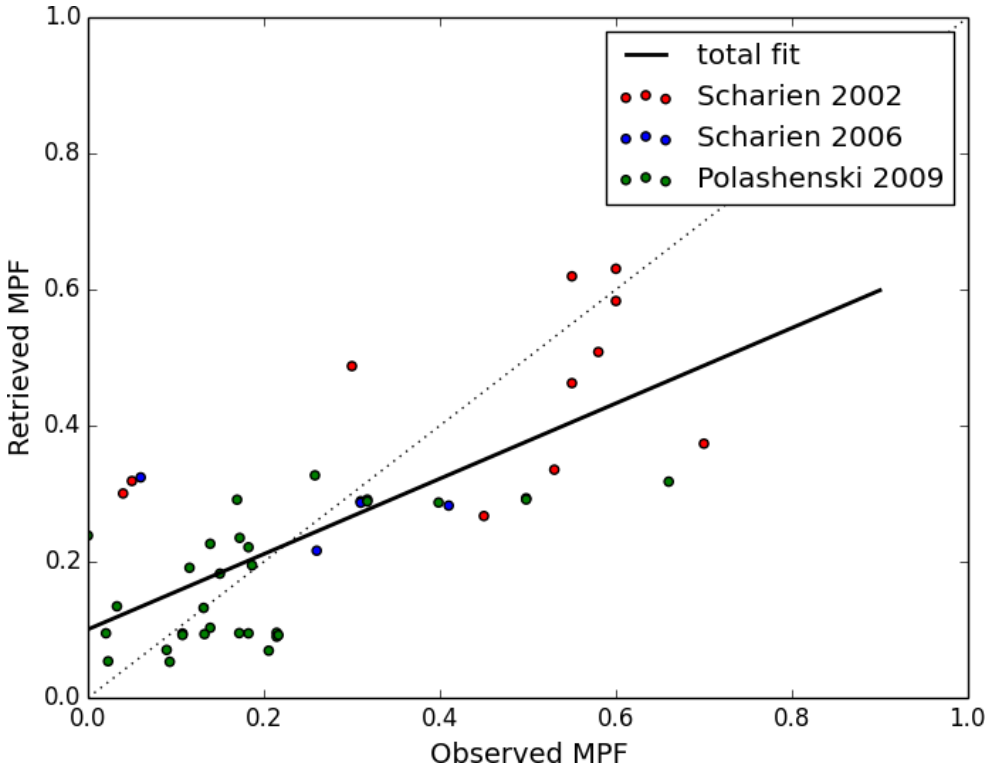

Figure 19. Three in situ campaigns on landfast ice: Scharien 2002 (red dots), Scharien 2006 (blue dots) and Polashenski 2009 (green dots). Total point number N = 47, RMS = 0.14, R^2 = 0.52. The overestimation of the low MPF may be connected to unscreened thin clouds which depending on the illumination-observation geometry may appear darker than the ice and therefore cause higher retrieved MPF.